

# Design and Control of a Three-Axis Serial-Kinematic High-Bandwidth Nanopositioner

Brian J. Kenton and Kam K. Leang, *Member, IEEE*

**Abstract**—The development of a high-performance three-axis serial-kinematic nanopositioning stage is presented. The stage is designed for high-bandwidth applications that include video-rate scanning probe microscopy and high-throughput probe-based nanofabrication. Specifically, the positioner employs vertically stiff, double-hinged serial flexures for guiding the motion of the sample platform to minimize parasitic motion (runout) and off-axis effects compared to previous designs. Finite element analysis (FEA) predicts the dominant resonances along the fast ( $x$ -axis) and slow ( $y$ -axis) scanning axes at 25.9 and 6.0 kHz, respectively. The measured dominant resonances of the prototype stage in the fast and slow scanning directions are 24.2 and 6.0 kHz, respectively, which are in good agreement with the FEA predictions. In the  $z$ -direction, the measured dominant resonance is approximately 70 kHz. The lateral and vertical positioning ranges are approximately  $9\ \mu\text{m} \times 9\ \mu\text{m}$  and  $1\ \mu\text{m}$ , respectively. Four approaches to control the lateral motion of the stage are evaluated for precision tracking at high-scan rates: 1) open-loop smooth inputs; 2) PID feedback; 3) discrete-time repetitive control implemented using field-programmable gate array (FPGA) hardware; and 4) model-based feedforward control. The stage is integrated with a commercial scan-by-probe atomic force microscope (AFM) and imaging and tracking results up to a line rate of 7 kHz are presented. At this line rate, 70 frames/s atomic force microscope video ( $100 \times 100$  pixels resolution) can be achieved.

**Index Terms**—Atomic force microscopy, compliant mechanisms, control systems, high-speed electronics, nanopositioning, piezoelectric actuators, scanning probe microscopy.

## I. INTRODUCTION

MULTIAXIS nanopositioning stages are critical in applications such as atomic force microscope (AFM) imaging, fiber optic alignment, and micro- and nanomachining. Particularly, video-rate scanning probe microscopy (SPM) [1] and high-throughput probe-based nanofabrication require nanopositioners capable of fast and accurate movements. Control methods such as feedforward- and feedback-based techniques can be employed to improve the operating bandwidth of nanopositioners [2], [3]. However, significant improvement in operating bandwidth (particularly in the kilohertz range) can be achieved by the development of mechanically stiff stages driven by piezo-stack actuators. Through careful mechanical design,

Manuscript received April 23, 2010; revised July 27, 2010; accepted November 21, 2010. Date of publication February 17, 2011; date of current version January 20, 2012. Recommended by Technical Editor G. Yang. This work was supported in part by the Nevada NASA Space Grant Consortium and in part by the National Science Foundation under Grant CMMI 0910570.

The authors are with the Mechanical Engineering Department, University of Nevada, Reno, NV 89557-0312 USA (e-mail: kam@unr.edu).

Color versions of one or more of the figures in this paper are available online at <http://ieeexplore.ieee.org>.

Digital Object Identifier 10.1109/TMECH.2011.2105499

TABLE I  
SUMMARY OF COMMON NANOPOSITIONING DESIGNS

Configuration	Range ( $\mu\text{m}$ )	Dominant Res. (kHz)	Imaging/line rate (range)
Tube scanner [4]	125 ( $x/y$ )	0.71 ( $x$ ) 0.70 ( $y$ )	122 lines/s ( $13.5 \times 13.5\ \mu\text{m}$ )
Tube scanner Dual stage ( $z$ ) [5]	n/a	6.35 ( $x/y$ ) 80 ( $z$ )	3 lines/s ( $25\ \mu\text{m}$ )
Tube scanner Dual stage ( $z$ ) [6]	100 ( $x/y$ ) 10 ( $z$ )	0.68 ( $x/y$ ) 23 ( $z$ )	6.25 lines/s ( $25 \times 25\ \mu\text{m}$ )
Shear piezo [8]	0.3 ( $x/y$ ) 0.20 ( $z$ )	$\sim 64$ >100	80 frames/s ( $128 \times 128\ \text{px}$ )
Flexure guided [11]	1 ( $x$ ) 3 ( $y$ ) 2 ( $z$ )	45 360 ("self")	33 frames/s ( $100 \times 100\ \text{px}$ )
Tuning fork ( $x$ ) Flexure guided ( $y$ ) [9]	<1 ( $x$ ) 2 ( $y$ )	100 40	1000 frames/s ( $100 \times 100\ \text{px}$ )
Flexure guided [12]	13 ( $x/y$ ) 4.3 ( $z$ )	>20 33	7810 lines/s (n/a)
Flexure guided [13]	25 ( $x/y$ )	2.73	n/a

performance-degrading off-axis and out-of-plane motion can be minimized. Herein, the design and control of a three-axis serial-kinematic nanopositioning stage that incorporates uniquely designed compliant flexures is presented. The serial-kinematic design is chosen for scanning-type applications, where one axis is chosen for high-speed scanning while the other is designed for low-speed motion.

Table I summarizes a collection of existing multi-axis nanopositioner designs. One of the simplest and most effective ways to achieve three-axis motion is to employ sectorized tube-shaped piezoelectric actuators [4]. However, the mechanical resonance of piezoelectric tube scanners is typically less than 1 kHz in the lateral scan directions, thus limiting the scan speed [4]–[7]. Additionally, the mechanical cross coupling causes undesirable SPM image distortion [7]. In general, the maximum open-loop (without compensation) positioning bandwidth is 1/100th to 1/10th of the dominant resonance [2]. Shear piezos because of their geometry have high mechanical resonances [8]. The major drawback of shear-type piezoactuators is that they provide limited range, typically less than  $1\ \mu\text{m}$ . Tuning forks have been implemented in both sample scanning and probe scanning SPMs [9]. The tuning-fork-based sample scanners are mechanically simple, but the small dimensions of the quartz tuning fork limit the scan range and the scanning motion is typically sinusoidal. Flexure-guided piezoactuated scanning stages [10], both direct drive serial-kinematic [1], [11] and parallel-kinematic [12] configurations, have been developed for high-speed purposes.

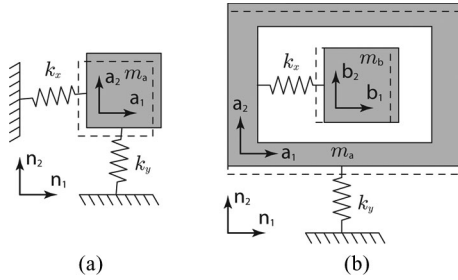


Fig. 1. (a) Parallel- and (b) serial-kinematic motion mechanisms.

The advantages of flexure-guided scanners are high mechanical resonances and low cross coupling. Multiple piezoactuators per degree-of-freedom (DF) have been used to increase range and bandwidth, but at the cost of increasing the power to drive the piezoactuators at high frequencies [1], [12]. Designs that involve mechanical amplification have been implemented to increase range without having to increase the actuator's length [10], [13]. However, the added mass of the mechanical amplifier along with the flexible linkages lowers the mechanical resonance. In general, a tradeoff must be made between range and bandwidth.

Motivated by the previous work [11], the main contribution of this paper is the design and control of a three-axis, serial-kinematic high-speed nanopositioning stage that offers approximately  $9 \mu\text{m} \times 9 \mu\text{m} \times 1 \mu\text{m}$  range of motion and kilohertz bandwidth. The proposed design employs a vertically stiff flexure geometry to increase the out-of-plane stiffness, thus reducing the effects of cross coupling (from  $x/y$  to  $z$ ). Additionally, the stage's out-of-plane stiffness is further improved by increasing the quantity of flexures  $n$ , decreasing the length  $L$  of each flexure, and thickening each flexure's center cross section. This study examines in detail the effects of varying these parameters. Along the vertical axis ( $z$ ), a novel plate flexure guides the motion of the sample stage to minimize the effects of bending modes in the vertical piezoactuator. Bending modes can significantly limit the positioning speed by causing the sample platform to rock side-to-side. It is pointed out for scanning-type applications, one lateral axis operates much faster than the other, and thus the serial-kinematic configuration is well suited for these types of applications [1], [9], [11]. The design of the stage, as well as the drive electronics and control software, are described. The prototype stage is integrated with a commercial SPM (NanoSurf easyScan 2 AFM with a maximum line rate of 10 Hz) to demonstrate improved scan speed with line rates up to 7 kHz. Four approaches to control the lateral motion of the stage are evaluated for precision tracking at high-scan rates.

## II. SERIAL-KINEMATIC NANOPositionERS

Serial- and parallel-kinematic configurations as shown in Fig. 1 are used for multi-axis nanopositioning, where  $k_x$  and  $k_y$  model the effective stiffness of the actuator along the  $x$ - and  $y$ -directions, respectively. The effective damping, omitted for brevity, in general appears in parallel with each spring element. The advantages of a parallel-kinematic configuration are that runout can easily be measured and corrected for [14], [15], and if both axes have the same mechanical bandwidth, the scan di-

rection can be chosen arbitrarily [12]. However, for raster-type scanning, the motion along one axis is considerably faster than the other. For example, to acquire an  $n \times n$ -pixels image in SPM, motion along the  $x$ -axis is  $n$ -times faster than the  $y$ -axis. For this reason, a serial-kinematic design with one high-speed stage is sufficient and may be more cost-effective to design and manufacture. Particularly, only the high-speed axis requires a costly high-bandwidth, high-power piezo-amplifier. Recently, serial-kinematic nanopositioners have been considered for high-speed SPM applications [1], [9], [11]. One disadvantage, however, is the inability to measure (and correct for) parasitic motion such as runout or guiding error. Instead, low runout is achievable with properly designed flexures and mechanisms for guiding the motion of the sample stage.

At low operating frequencies, a simple beam flexure is effective at guiding the motion of the platform and minimizing parasitic motion [11]. At high frequencies, both in- and out-of-plane resonant modes can be excited due to lack of stiffness along the out-of-plane directions, thus limiting the positioning speed. This is one of the major challenges in designing serial-kinematic stages, particularly because the bending (out-of-plane) modes are easily excited as the piezoactuator is much stiffer in the actuation direction. Dominant resonances occurring in the actuation direction are tolerable compared to out-of-plane modes; preferably, if the actuation modes precede the out-of-plane or off-axis modes. To ensure this, the compliant flexures are designed to have high out-of-plane stiffness, while being sufficiently soft in the actuation direction to avoid affecting the achievable stroke of the piezoactuator [1], [16]. The mechanical stiffness can be improved by selecting piezoactuators with large cross-sectional area, but the overall capacitance also increases, and thus the required power to drive the actuator at high speed also increases. The most practical approach is to focus on improving the design of the flexures such that they are sufficiently stiff along the off-axis directions.

A first-generation serial-kinematic two-axis nanopositioner based on simple beam flexures and consisting of multiple parts and assembled using fasteners is shown in Fig. 2(a1) and (a2) [11]. The high-bandwidth  $x$ -axis is nested within the low-speed  $y$ -axis. The measured first resonances in the  $x$ - and  $y$ -axes are 29 and 1.5 kHz, respectively [11]. Since the stage consisted of many parts assembled together to create the complete system, slight misalignment during assembly caused incorrect preload on the flexures and the piezoactuator. And thus, the stage's dynamic response was sensitive to the assembly process and variations in the boundary conditions.

An improved design is shown in Fig. 2(b). The stage body is manufactured from 7075 aluminum using the wire electrical discharge machining (EDM) process to create a monolithic platform. Positioning of the sample in the vertical direction is achieved using a piezo-stack actuator embedded into the  $x$ -positioning stage [1]. The dominant resonances in the  $x$ - and  $y$ -axes are measured at 10 and 2.4 kHz, respectively.

In the following, a new serial-kinematic nanopositioning stage is proposed that takes advantage of the monolithic design, has compliant flexures with improved vertical stiffness to minimize out-of-plane motion, and consists of strategically

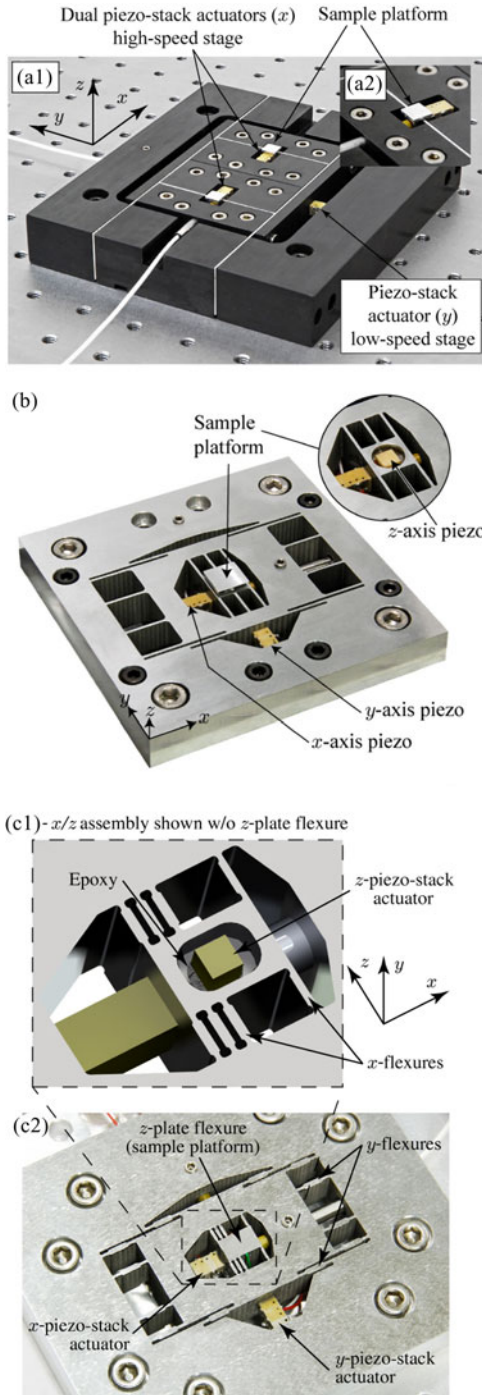


Fig. 2. Serial-kinematic nanopositioners. (a1) First-generation two-axis design, high-speed stage ( $x$ ) is nested inside of the low-speed stage ( $y$ ) [11]. (b1) Sample platform and  $x$ -axis piezo-stack actuator. (b) Second-generation three-axis design. Third-generation three-axis design: (c1)  $x/z$  stage assembly with vertically stiffened flexures and (c2) full stage body with the high-speed  $x$ - and low-speed  $y$ -axes and vertically stiffened flexures.

placed flexures to minimize the sample platform's tendency to rotate ( $\theta_x, \theta_y, \theta_z$ ) at high frequencies. Also, the stage is designed to ensure that the first resonance in all three axes are axial (actuation or piston) modes, rather than off-axis modes that can severely limit performance. A functioning prototype is shown in

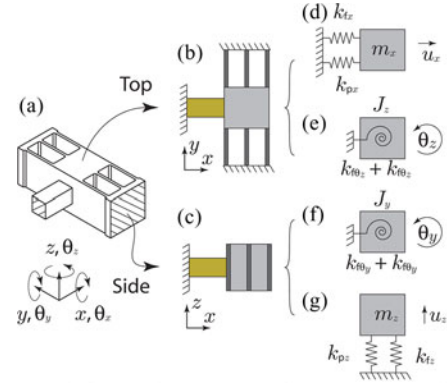


Fig. 3. Generic flexure-guided stage simplified to single DF systems modeling the dominant modes.

Fig. 2(c1) and (c2), and the details of the design, performance, and application in AFM imaging are described next.

### III. MECHANICAL DESIGN FOR HIGH PERFORMANCE

#### A. Mechanical Stiffness

For translational motion  $u_i$  ( $i = x, y, z$ ), the single DF mechanical resonance is given by  $f_{u_i,0} = 1/2\pi\sqrt{k_i/m_i}$ , where  $m_i$  and  $k_i$  are the effective translational mass and stiffness, respectively. Likewise for rotational motion  $\theta_i$  ( $i = x, y, z$ ), the first resonance is  $f_{\theta_i,0} = 1/2\pi\sqrt{k_{\theta_i}/J_i}$  where  $J_i$  and  $k_{\theta_i}$  are the effective mass moment of inertia and rotational stiffness, respectively. To ensure that actuation modes occur before the out-of-plane modes, the strategy taken is to optimize the stage geometry and flexure configuration so that the out-of-plane stiffness-to-mass ratios ( $k_z/m_z, k_{\theta_y}/J_y, k_{\theta_z}/J_z$ ) are higher than the actuation stiffness-to-mass ratio  $k_x/m_x$ . Fig. 3 shows the simplification of a high-speed  $x$ -stage [see Fig. 2(c1)] into single DF systems to model four of the dominating resonance modes. The top and side views are broken down to show the effective springs and masses affecting the body for (d) actuation  $u_x$ , (e) and (f) rotation  $\theta_z$  and  $\theta_y$ , and (g) vertical  $u_z$  modes. Damping is omitted for convenience.

#### B. Piezo-Stack Actuator

Piezo-stack actuators are stiff and compact; thus, they have high mechanical resonances. A comparison of four plate-stack piezoactuators (Noliac) of varying cross-sectional areas is shown in Table II. Each actuator in this comparison is 10 mm long and meets the desired free stroke of 11  $\mu\text{m}$ . (A small percentage of the free stroke will be lost due to flexure stiffness and boundary conditions associated with gluing the piezo-stack to the stage during assembly.) The capacitance increase is nearly proportional to the cross-sectional area with an average of 15.5 nF/mm<sup>2</sup> (for a 10-mm long piezo-stack actuator). The Young's modulus is calculated from the blocking force and free stroke. For instance, the Young's modulus of a 5 mm  $\times$  5 mm  $\times$  10 mm piezoactuator is determined to be 33.9 GPa [11]. As shown in Table II, higher actuation and out-of-plane stiffness

TABLE II  
COMPARISON OF PLATE-STACK PIEZOACTUATORS

Size (mm)	Free stroke ( $\mu\text{m}$ )	Cap. (nF)	$k_a$ N/ $\mu\text{m}$	$k_z^*$ N/ $\mu\text{m}$	$k_z/k_a$
3x3x10	11.15	114	30.5	2.0	0.066
5x5x10	11.78	387	84.8	10.7	0.126
7x7x10	12.09	835	166.1	28.0	0.169
10x10x10	12.13	1673	339.0	69.2	0.204

\*Stiffness for fixed-guided beam accounting for shear (see Section III-C).

can be obtained by using larger (cross section) piezo-stacks. The cost, however, is higher capacitance that increases the net power to drive the actuators, especially at high frequencies.

The stiffness in the actuation direction is maximized by using the piezoactuator in direct-drive configuration. Although mechanical displacement amplification is an effective way to increase resultant stage displacement, the added mass and reduced actuation stiffness reduces actuation resonance values [10], [13], [17]. When used in direct drive, the mechanical properties of the piezoactuator can be exploited to aid in increasing out-of-plane resonances [1], [12].

### C. Flexure Design for Lateral Positioning ( $x/y$ )

The vertical stiffness of the  $x$ - and  $y$ -stages is increased by: 1) increasing the number of flexures; 2) utilizing shorter (effective length) flexures; and 3) converting the flexures from constant rectangular cross section beam flexures to a serial-compliant double-hinged flexure with a “rigid” center connecting link (see Fig. 6). The first step taken to increase the flexure stiffness in the vertical direction is studying how the total number of flexures  $n$  used in parallel, flexure thickness  $t$ , and length  $L$  affect the vertical stiffness  $k_z$  for a given actuation stiffness  $k_a$ . This comparison is done analytically using finite element analysis [COSMOSWorks finite element analysis (FEA)].

The stiffness of a flexure is defined as the ratio of a load  $F$  and the resulting displacement  $u$ . The displacements and loads are translational displacement  $u_i$ , rotational displacement  $\theta_i$ , translational force  $F_i$  acting on a point in the  $i$ -direction, and moment  $M_i$  (torque  $T$ ) acting about the  $i$ -axis  $\theta_i$ , respectively, where  $i = x, y, z$ . Fig. 4(a) illustrates the corresponding directions of the displacements and loads acting on the free end of a fixed/free cantilever beam which models a beam flexure. The in- and out-of-plane compliances for a fixed/free beam are derived using Castigliano’s second theorem [18]–[20]. The compliance equations are then used to derive equations for the actuation and vertical stiffness  $k_i$  of a fixed/roller guided beam shown in Fig. 4(b) through (d). In the second-generation design [see Fig. 2(b)], the fillet radius is considerably smaller compared to the flexure length and therefore has minimal effect on the flexure stiffness. For this reason, to simplify the flexure stiffness equations in this initial analysis, the compliance equations are derived for a beam with a constant cross-sectional thickness.

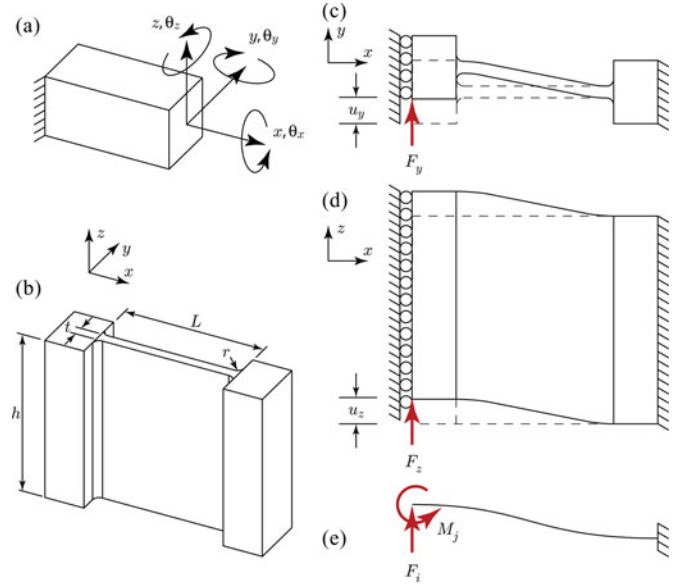


Fig. 4. Compliant beam: (a) fixed/free cantilever beam shown with the applied loads and displacements at the free end. Corner-tilted beam flexure: (b) isometric view, (c) top and (d) side views showing displacement caused by force  $F_i$ , for  $i = x, y$ , in a fixed/guided end configuration. (e) Loads acting on the free end of a fixed/free beam.

For a fixed/free beam of rectangular cross section, the total strain energy is

$$U = U_{\text{axial}} + U_{\text{torsion}} + U_{\text{bending}} + U_{\text{shear}}$$

$$U = \int_0^L \left[ \frac{F^2}{2AE} + \frac{T^2}{2GJ} + \frac{M^2}{2EI} + \frac{\alpha V^2}{2GA} \right] dx \quad (1)$$

where  $L$  is the beam length,  $A$  is the cross-sectional area of the beam,  $h$  is the height,  $t$  is the thickness,  $E$  is Young’s modulus,  $G = E/2(1 + \nu)$  is the shear modulus,  $\nu$  is Poisson’s ratio,  $J = ht^3[(1/3) - 0.21(t/h)(1 - (t^4/12h^4))]$  is the approximate torsional moment of inertia [21],  $I = ht^3/12$  is the second moment of inertia about the vertical  $z$ -axis,  $V$  is the shear force, and  $\alpha$  is a shape factor for the cross section used in the shear equation (for a rectangular cross section  $\alpha = 6/5$ ) [20]–[22].

Applying Castigliano’s second theorem, the displacement of a point in a given direction  $u_i$ ,  $\theta_i$  is the partial derivative of the total strain energy with respect to the applied force, i.e.,

$$u_i = \frac{\partial U}{\partial F_i}; \quad \theta_i = \frac{\partial U}{\partial M_i}. \quad (2)$$

From here, the compliance is simply found by dividing the displacement by the applied load, i.e.,

$$C_{u_i, F_j} = \frac{u_i}{F_j}; \quad C_{\theta_i, M_j} = \frac{\theta_i}{M_j}. \quad (3)$$

For example, the compliance of the rectangular cross section fixed–free beam in Fig. 4(a) due to a point load in the  $y$  direction starts with the total strain energy

$$U = \int_0^L \frac{M(x)^2}{2EI(x)} dx + \int_0^L \frac{\alpha V(x)^2}{2GA(x)} dx \quad (4)$$

where  $A(x)$  and  $I(x)$  are constants. The coordinate system is placed on the free end of the flexure as shown in [19] where the shear is  $V(x) = F_y$  and the moment is  $M(x) = F_y x$ . The total strain energy for the applied load is

$$\begin{aligned} U &= \frac{F_y^2}{2EI} \int_0^L x^2 dx + \frac{\alpha F_y^2}{2GA} \int_0^L dx \\ &= \frac{F_y^2 L^3}{6EI} + \frac{\alpha F_y^2 L}{2GA}. \end{aligned} \quad (5)$$

Therefore, the resultant displacement is

$$u_y = \frac{\partial U}{\partial F_y} = \frac{F_y L^3}{3EI} + \frac{\alpha L F_y}{GA} \quad (6)$$

and the compliance is

$$C_{22} = \frac{u_y}{F_y} = \frac{L^3}{3EI} + \frac{\alpha L}{GA}. \quad (7)$$

The compliances are then used to form the compliance matrix  $\mathbf{C}$  which is defined as the ratio of the displacement  $\mathbf{U} = [x \ y \ \theta_z \ z \ \theta_y \ \theta_x]^T$  for a given load  $\mathbf{L} = [F_x \ F_y \ M_z \ F_z \ M_y \ M_x]^T$ ; hence, the displacement vector is

$$\begin{pmatrix} u_x \\ u_y \\ \theta_z \\ u_z \\ \theta_y \\ \theta_x \end{pmatrix} = \begin{bmatrix} C_{11} & 0 & 0 & 0 & 0 & 0 \\ 0 & C_{22} & C_{23} & 0 & 0 & 0 \\ 0 & C_{23} & C_{33} & 0 & 0 & 0 \\ 0 & 0 & 0 & C_{44} & C_{45} & 0 \\ 0 & 0 & 0 & C_{45} & C_{55} & 0 \\ 0 & 0 & 0 & 0 & 0 & C_{66} \end{bmatrix} \begin{pmatrix} F_x \\ F_y \\ M_z \\ F_z \\ M_y \\ M_x \end{pmatrix}.$$

For a constant cross section fixed/free beam, the compliances are  $C_{11} = L/AE$ ,  $C_{22} = L^3/3EI + \alpha L/GA$ ,  $C_{23} = L^2/2EI$ ,  $C_{33} = L/EI$ ,  $C_{44} = 4L^3/Eh^3t + \alpha L/GA$ ,  $C_{45} = 6L^2/Eh^3t$ ,  $C_{55} = 12L/Eh^3t$ , and  $C_{66} = L/GJ$ . For a long slender beam, shear strain has little effect and therefore can be ignored in  $C_{22}$ . For a short beam with a significant height-to-length aspect ratio, such as the vertical displacement of the flexure shown in Fig. 4(d), much of the deflection is in shear, and therefore cannot be ignored. The displacement vector equation presented earlier is used to solve for the actuation stiffness  $k_y$  and vertical stiffness  $k_z$  of a fixed/guided flexure beam, i.e.,  $F_i/u_i = k_i$ . Torsional stiffness is not investigated because the  $\theta_x$  rotational mode is largely dependent upon the vertical flexure stiffness when the flexures are placed at the corners of the stage body as mentioned in Section III-D. Fig. 4(e) shows the applied load and the expected deflection curve of the flexure in both (c) the actuation direction and (d) the vertical direction. The active load being applied to the flexure is the in-plane force  $F_i$ . The resultant moment  $M_j = -F_i L/2$  is caused by the roller-guided end constraint. Therefore, the flexure displacement in the actuation direction  $u_y$  due to the applied force  $F_y$  and moment  $M_z = -F_y L/2$  is

$$\begin{aligned} u_y &= C_{22} F_y + C_{23} M_z = C_{22} F_y - C_{23} F_y L/2 \\ &= F_y \left[ \frac{L^3}{3EI} + \frac{\alpha L}{Ght} - \frac{L}{2} \frac{L^2}{2EI} \right]. \end{aligned} \quad (8)$$

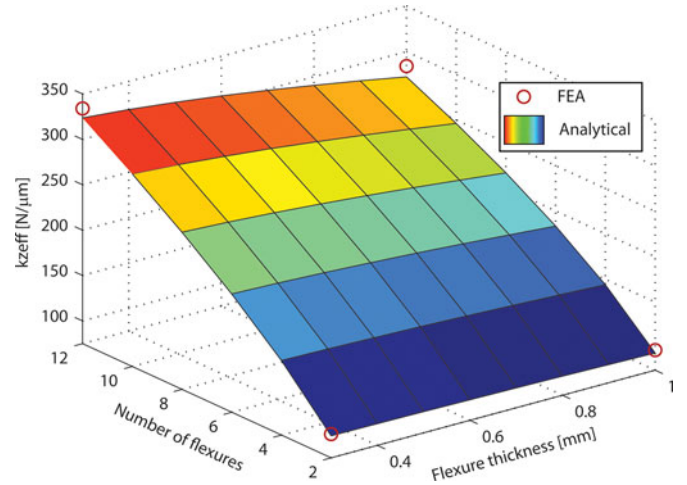


Fig. 5. FEA and analytical results showing effective vertical flexure stiffness  $k_{z,eff}$  with respect to the flexure thickness  $t$  and quantity of flexures  $n$ . Effective actuation stiffness  $k_{y,eff}$  is held constant at  $10 \text{ N}/\mu\text{m}$ .

Taking the ratio of the applied load to the displacement, the actuation stiffness (neglecting shear) is

$$k_y = \frac{F_y}{u_y} = \left[ \frac{L^3}{12EI} + \frac{\alpha L}{Ght} \right]^{-1} \cong \frac{12EI}{L^3}. \quad (9)$$

Using the same method, the displacement of the flexure in the vertical direction  $u_z$  is

$$\begin{aligned} u_z &= C_{44} F_z + C_{45} M_y = C_{44} F_z - C_{45} F_z L/2 \\ &= F_z \left[ \frac{4L^3}{Eh^3t} + \frac{\alpha L}{Ght} - \frac{L}{2} \frac{6L^2}{Eh^3t} \right]. \end{aligned} \quad (10)$$

Similarly, the vertical stiffness is

$$k_z = \left[ \frac{L^3}{Eh^3t} + \frac{\alpha L}{Ght} \right]^{-1}. \quad (11)$$

Because of the high aspect ratio in the vertical direction, shear cannot be ignored.

Equations (9) and (11) are used to study the effect of the quantity of flexures  $n$  and flexure thickness  $t$  on the effective vertical out-of-plane stiffness  $k_{z,eff}$ . To do this, the desired actuation stiffness  $k_{y,eff} = 10 \text{ N}/\mu\text{m}$  was divided among the number of flexures  $n$  to give the actuation stiffness for an individual flexure  $k_{yi}$ . From there, (9) is used to determine the length  $L$  for  $t \in [0.3, 1]$  mm. The individual vertical stiffness  $k_{zi}$  is then calculated using (11). The effective vertical stiffness is  $k_{z,eff} = \sum^n k_{zi}$ . By increasing the number of flexures from 2 to 12 (1 mm thick), the vertical stiffness is increased from 93.9 to 272  $\text{N}/\mu\text{m}$  (190% increase). For  $n = 2$ , decreasing the flexure thickness from 1 to 0.3 mm thick (which effectively decreases the flexure length) increased the vertical stiffness from 93.9 to 99.3  $\text{N}/\mu\text{m}$  (5.78% increase). Increasing the number of flexures from 2 to 12 and decreasing the flexure thickness from 1 to 0.3 mm thick produces a vertical stiffness of 324  $\text{N}/\mu\text{m}$  (245% increase). In Fig. 5, the circles denote the  $k_{z,eff}$  values obtained using FEA. The FEA results follow the trend of the analytical results with the only variance being an increase in effective

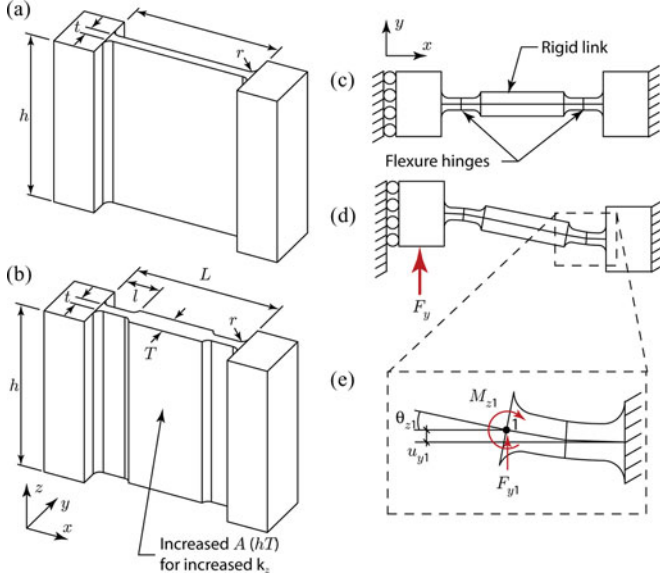


Fig. 6. Beam flexure design: (a) trimetric view of constant cross section corner-filletted flexure beam, (b) trimetric view of corner-filletted serial-compliant flexure, (c) top view, (d) top view with applied load, and (e) expanded view of corner-filletted flexure hinge.

stiffness (average increase = 3.15%). Increasing flexure height  $h$  also contributes to increasing vertical stiffness but at the cost of a taller stage body, which increases the mass  $m$  thus reducing the actuation resonance.

The most dramatic increase in vertical stiffness for a beam flexure is observed by increasing the number of flexures  $n$ . Decreasing the flexure thickness (and as a result the flexure length) increases the vertical stiffness as well. But the limiting factor of decreasing the flexure thickness is stress. A shorter thinner beam flexure will have higher stress concentration than a longer thicker beam flexure of equal stiffness.

When a corner-filletted beam flexure, as studied earlier, is displaced in the actuation direction, the majority of the strain is located at the flexure ends near the fillets. Additionally, when the same flexure is displaced in the vertical direction, the majority of the vertical displacement is in shear strain located at the center cross section. An effective way to further increase the out-of-plane stiffness of a beam flexure is to increase the thickness of the center section of the flexure, thus converting the beam flexure into a double-hinged serial flexure as shown in Fig. 6(b). Both analytical and FEA methods are used to study the vertical stiffness of the “thickened” flexures. The cross-sectional area and second moment of inertia values in (4) are replaced with  $A(x) = ht(x)$  and  $I(x) = ht(x)^3/12$ , respectively. For example, the thickness of the flexure in Fig. 6(b) is

$$t(x) = \begin{cases} t + 2[r - \sqrt{x(2r - x)}], & x \in [0, a] \\ t, & x \in [a, b] \\ t + 2[r - \sqrt{(l - x)(2r - l + x)}], & x \in [b, c] \\ t + 2r, & x \in [c, d] \\ t + 2[r - \sqrt{(l - g)(2r - l + g)}], & x \in [d, e] \\ t, & x \in [e, f] \\ t + 2[r - \sqrt{g(2r - g)}], & x \in [f, L] \end{cases} \quad (12)$$

TABLE III  
y-AXIS FLEXURE STIFFNESS COMPARISON

Type	$k_{y \text{ eff}} (N/\mu m)$		$k_{z \text{ eff}} (N/\mu m)$	
	Analytical	FEA	Analytical	FEA
Filletted beam	5.85	6.00	237.7	213.9
Thickened center	5.86	5.32	283.5	238.2

where  $a = r, b = l - r, c = l, d = L - l, e = d + r, f = L - r, g = L - x, t$  and  $l$  are thickness and length of the thin section of the flexure,  $r$  is the fillet radius,  $t + 2r = T$  is the thickness of the thickened section, and  $L$  is the length of the entire flexure. For this case, the compliance is determined by first determining the total strain energy (4) while using the thickness function  $t(x)$  in the area  $A(x)$  and second moment of inertia  $I(x)$  expressions. Again, the coordinate system is placed on the free end for simplification and to allow for direct integration as shown in [19]. For instance, the total strain energy for bending due to a point load is

$$U = \int_0^L \frac{M(x)^2}{2E[ht(x)^3]/12} dx + \int_0^L \frac{\alpha V(x)^2}{2Ght(x)} dx \\ = \frac{12F_y^2}{2Eh} \int_0^L \frac{x^2}{t(x)^3} dx + \frac{\alpha F_y^2}{2Gh} \int_0^L \frac{1}{t(x)} dx. \quad (13)$$

Taking the partial derivative with respect to the applied force  $F_y$  gives the displacement

$$u_y = \frac{\partial U}{\partial F_y} = \frac{12F_y}{Eh} \int_0^L \frac{x^2}{t(x)^3} dx + \frac{\alpha F_y}{Gh} \int_0^L \frac{1}{t(x)} dx. \quad (14)$$

The in-plane (and out-of-plane) stiffness is then calculated numerically by taking the ratio of the force to deflection. Table III compares the actuation and vertical stiffness of a standard filletted flexure beam to a thickened flexure beam obtained analytically and using FEA. This comparison shows how the vertical stiffness of beam flexures similar to the ones used on the  $y$ -stage can be increased an additional 19.3% by simply increasing the thickness of the center section. To keep the actuation stiffness  $k_{y \text{ eff}}$  constant, the length  $L$  of the thickened flexure is increased from 9.75 to 10.70 mm.

In summary, the effective vertical stiffness can be improved to increase the out-of-plane stiffness by 1) increasing the number of flexures  $n$ ; 2) decreasing the flexure length  $L$ ; and 3) thickening the center section of a beam flexure to create a serial-compliant double-hinged flexure.

#### D. Flexure Placement to Minimize Rotation

Flexure placement is important to help increase rotational stiffness. Increasing the length (and width) of a stage and placing flexures at the corners of the moving platform increase rotational stiffness of the platform. However, the cost of increasing the size of the platform is increasing overall mass, thus lowering the mechanical resonance.

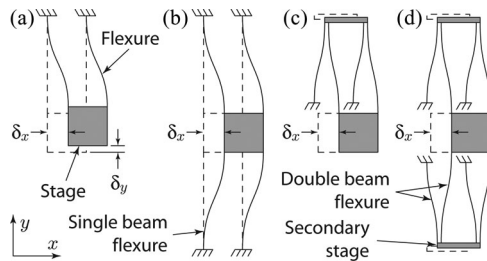


Fig. 7. Flexure-guided stages: guided by (a) two single-beam flexures on one side of the drive axis, (b) four single-beam flexures symmetric about the drive axis, (c) one double parallelgram flexure module, and (d) two double parallelgram flexure modules symmetric about the drive axis.

### E. Stress Stiffening

When single-beam flexures [see Fig. 7(a)] are used symmetrically about the drive axis such as in the  $x$ - and  $y$ -stages [see Fig. 7(b)], large displacements will cause stress stiffening and therefore restrict range of motion [14], [23]. To allow for larger displacements, double beam flexures or double parallelgram flexures should be used [15], [24] as shown in Fig. 7(c) and (d). The cost of using multiple beam flexures in series is reduced out-of-plane stiffness, which lowers the mechanical resonances. Because the stages in this specific design have relatively small displacements relative to the flexure length and thickness (worst case of  $10\text{-}\mu\text{m}$  displacement for  $7\text{-mm}$  long by  $0.4\text{-mm}$  thick flexure) stress stiffening for single-beam flexures is minimal and therefore can be neglected. Additionally, because the stages are being specifically designed for high mechanical resonances, out-of-plane stiffness is critical. For this reason, single-beam flexures are used.

### F. Modal Analysis for $x/y$ -Stage

The first five modes for the  $x$ -,  $y$ -, and  $z$ -stages are predicted using the *frequency* tool in COSMOSWorks (FEA). (Detailed discussion of the  $z$ -stage design is presented later.) It is assumed that the resonances of the  $y$ -stage would not be excited by the dynamic motion of the inner nested  $x$ -stage. This allows the design shown in Fig. 8(a) to be broken down into the low-speed  $y$ -stage [see Fig. 8(b1)–(b5)], high-speed  $x$ -stage [see Fig. 8(c1)–(c5)], and vertical  $z$ -stage [see Fig. 8(d1)–(d5)]. The boundary faces of each stage (shown hatched) have a fixed boundary condition. All contacting components are bonded together with compatible mesh. The meshing is done at “high quality” with refined meshing at the flexure fillets and pivot points ( $0.25\text{ mm}$  minimum element size on surfaces). The materials used and their corresponding mechanical properties are as follows:

- 1) aluminum:  $E = 72\text{ GPa}$ ,  $\nu = 0.33$ ,  $\rho = 2700\text{ kg/m}^3$ ,
- 2) steel:  $E = 200\text{ GPa}$ ,  $\nu = 0.28$ ,  $\rho = 7800\text{ kg/m}^3$ ,
- 3) piezo-stack:  $E = 33.9\text{ GPa}$ ,  $\nu = 0.30$ ,  $\rho = 8000\text{ kg/m}^3$ ,  
and
- 4) alumina:  $E = 300\text{ GPa}$ ,  $\nu = 0.21$ ,  $\rho = 3960\text{ kg/m}^3$ ,

where the modulus for the piezo-stack was calculated from the stiffness and blocking force. The predicted first mechanical resonance for the  $y$ -,  $x$ -, and  $z$ -stages are  $5.96$ ,  $25.9$ , and  $113\text{ kHz}$ , respectively, all of which are in the corresponding stage ac-

tuation direction as preferred. Simulated FEA frequency response is done using the *Linear Dynamic (Harmonic)* tool in COSMOSWorks. A constant amplitude sinusoidal force is applied in the actuation direction at the corners of the piezoactuator/stage interfaces. The force generated is assumed proportional to the applied voltage. A global modal damping ratio of  $0.025$  is applied to simulate the damping of aluminum alloy and to produce a resonance peak of approximately  $20\text{ dB}$ . Fig. 12(a1) and (b1) shows the predicted frequency response plots for the  $x$ - and  $y$ -axes with the resonant peaks occurring at  $25.9$  and  $5.96\text{ kHz}$ , respectively.

### G. $z$ -Stage Design

The quick movements of the  $z$ -stage when tracking sample features under feedback control such as steps may excite the resonance modes of the nesting  $x$ -stage. To minimize impulsive forces along the vertical direction, a dual counterbalance configuration is utilized. Ando *et al.* [1] describe four configurations that include face mounting, mounting both faces of the actuator to flexures, and inserting the piezoactuator in a hole and allowing the end faces to be free. Dual face-mounted  $z$ -piezoactuators are a simple and effective method for counterbalancing. However, the disadvantage is the first resonance mode for a slender piezoactuator is bending as shown in Fig. 9(a1), instead of the desired actuation mode as illustrated in Fig. 9(a2). Inserting the piezoactuator into a hole in the  $x$ -stage is tested in the Generation 2 design shown in Fig. 2(b). Unfortunately, the design requires a long piezoactuator and did not constrain the end faces well.

A new configuration as shown in Fig. 10 is proposed in which a dual face-mounted piezo arrangement is combined with a compliant end-plate flexure. The piezoactuators are first recessed within the nesting stage so that the free face is flush with the top surface of the stage body. The plate flexure is glued to the free end of the piezoactuator and the surrounding surface of the stage. Fig. 9(b1) and (b2) shows how by using a plate flexure, the bending (and torsional) modes can be shifted above the frequency of the actuation mode.

## IV. FABRICATION, ASSEMBLY, AND CHARACTERIZATION

### A. Fabrication and Assembly

The main stage body is constructed from a single block of 7075 aluminum alloy, where the features are machined using traditional milling and wire EDM processes. The  $x$ - and  $y$ -stages are actuated with  $5\text{ mm} \times 5\text{ mm} \times 10\text{ mm}$  Noliac SCMAP07 piezo-stack actuators (see Section III-B), where the motion is guided by compliant, center-thickened flexures described earlier (see Section III-C). The  $x$ -flexures are designed to have a pivot point thickness of  $0.5 \pm 0.03\text{ mm}$  to produce an effective axial stiffness of  $14 \pm 2\text{ N}/\mu\text{m}$ . When assembling the  $x$ - and  $y$ -stages, it is important to preload the piezoactuators. Failure to preload will result in lower mechanical resonances that resemble the predicted free stage resonance (stage without piezoactuator). Preloading is accomplished by initially displacing the stages in the actuation direction, sliding the piezoactuators in place, and then applying shims and glue. The tension on the stage is then released onto the piezoactuator resulting in preload.

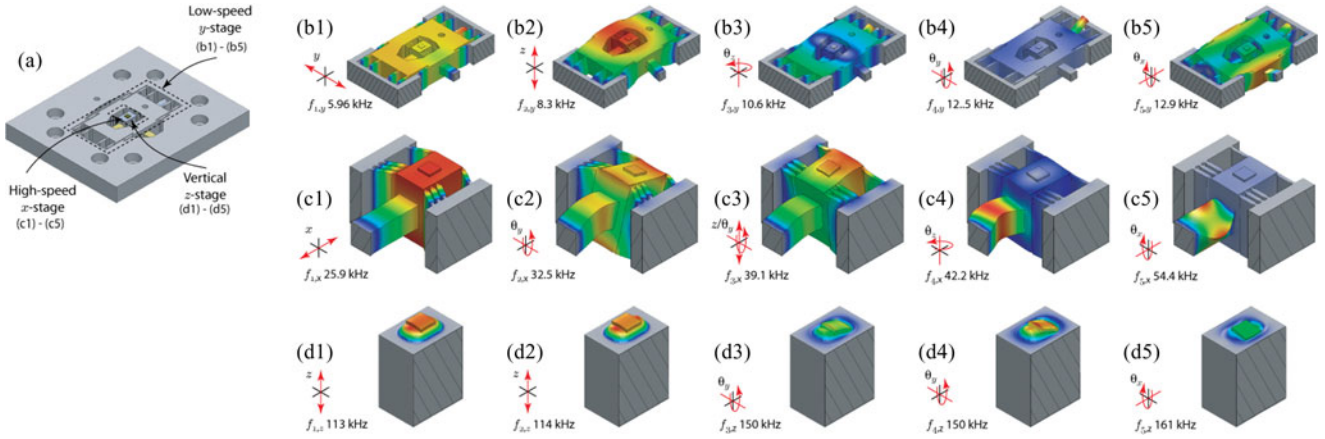


Fig. 8. Finite element analysis results showing first five modes: (a) high-speed scanning stage; (b1)–(b5) low-speed  $y$ -stage; (c1)–(c5) high-speed  $x$ -stage; and (d1)–(d5) vertical  $z$ -stage. Each stage section is designed to have the first mechanical resonance to occur in the actuation direction (i.e., piston mode).

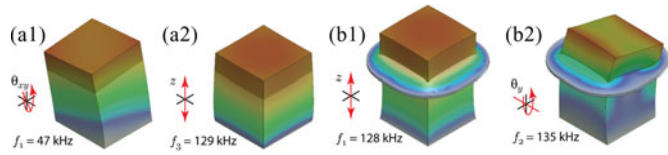


Fig. 9. FEA results for  $z$ -piezo with 1-mm thick sample: (a) without and (b) with flexure.

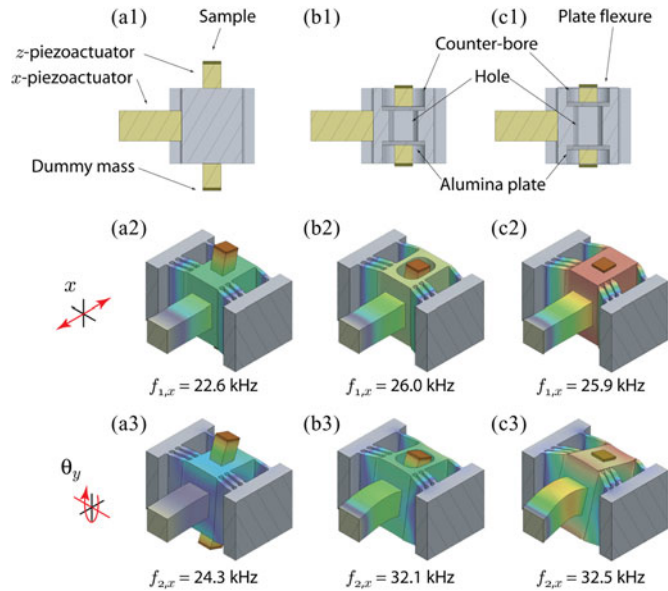


Fig. 10. Three configurations for the  $z$ -piezoactuator and corresponding first two modes. The dynamic characteristics of the face-mounted configuration in (a) are improved by (b) recessing the  $z$ -piezoactuator into the  $x$ -stage body and (c) adding a plate flexure to the free face of the  $z$ -actuator.

The  $z$ -stage is designed using two  $3 \text{ mm} \times 3 \text{ mm}$  Noliac SCMAP06 piezo-stack actuators. The actuators are recessed within the nested  $x$ -stage. The base of each actuator is glued to an alumina plate while the free end is constrained using plate flexures. To increase the stiffness of the piezoactuators, the plate-stacks are used without the stock 1-mm thick ceramic insulating end plates. Instead, the mounting face is insulated by

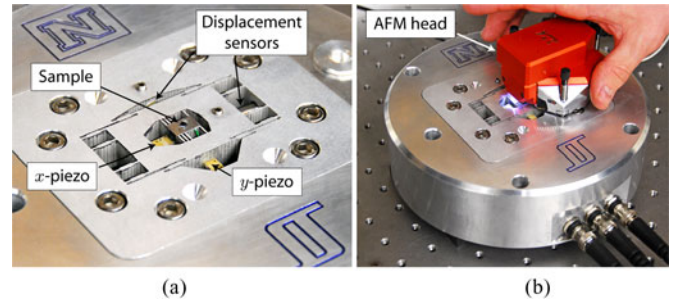


Fig. 11. Assembled positioner: (a) stage with sample glued to sample platform. Holes were machined into the stage body to accommodate inductive or capacitive sensors. The sensors are held in place with set screws as shown. (b) AFM head [Nanosurf, easyScan 2 ([www.nanoscience.com](http://www.nanoscience.com))] coupled with the positioning stage for high-speed AFM imaging experiments.

the alumina base plate, while the top surface is insulated from the plate flexure with a thin sheet of mica.

The experimental prototype is shown in Fig. 11 with the scanner body bolted to an aluminum base. To reduce mass, the sample (Mikromasch TGZ01) is cut to  $3 \text{ mm} \times 3 \text{ mm}$  and is glued directly to the sample platform [see Fig. 11(a)].

### B. Drive Electronics and SPM Imaging Software

The fast scanning axes,  $x$  and  $z$ , require drive electronics capable of supplying sufficient power to drive the capacitive piezoelectric loads at high frequency. The nominal capacitances for the  $x$ - and  $z$ -axis actuators are 380 and 100 nF, respectively. The piezo-amplifiers are built around the Power Amp Design ([www.powerampdesign.net](http://www.powerampdesign.net)) PAD129 power op-amp, with a gain bandwidth product of 1 MHz. A 200-V dc power supply is constructed from two linear regulated 100 V, 3 A dc power supplies (Acopian A100HT300) connected in series. The  $y$ -axis is driven by a custom-design PiezoDrive amplifier developed by Dr. A. J. Fleming.

A LabView program<sup>1</sup> is created to control the nanopositioning stage for high-speed SPM imaging. The program is compatible with National Instrument data acquisition cards that support the NI-DAQmx drivers, e.g., NI PCI-6115 high-speed simultaneous sampling data acquisition card. With such a card, up to 2.5 MS/s I/O bandwidth is achieved. At this rate, the user can record up to several seconds of  $160 \times 160$  pixels AFM images with line rates at 8 kHz (50 frames/s).

### C. Performance Characterization

The fabricated scanner shown in Fig. 11 is tested to determine the stiffness, maximum range, and dynamic characteristics. Prior to assembly, the effective stiffnesses of the  $x$ - and  $y$ -stages are determined by taking the ratio of the measured displacement due to an applied load. Static loads are applied to the stages by mounting the scanner vertically to a fixture ( $z$ -axis parallel to ground), running a cable through the hole in the  $x$ -stage and hanging masses from the cable. A total of 15 Lbf (66.7 N) is applied in the positive and negative directions in 2.5 Lbf (11.1 N) increments. Displacement is measured using a Kaman inductive sensor (SMU9000-15N). The analytical, FEA predicted, and measured stiffnesses are 7.82, 7.42, and 3.81 N/ $\mu\text{m}$ , respectively, for the  $x$ -stage and 4.28, 4.04, and 5.10 N/ $\mu\text{m}$ , respectively, for the  $y$ -stage. The discrepancy between the predicted and measured values is attributed to machining tolerances.

Application of 180-V peak-to-peak sine input at 10 Hz to the  $x$  and  $y$  piezoactuators resulted in 8.19  $\mu\text{m}$  and 8.34  $\mu\text{m}$  travel, respectively. Since the  $x$ - and  $y$ -axes can tolerate a maximum of 200 V, the maximum lateral range of the stage is approximately 9  $\mu\text{m} \times 9 \mu\text{m}$ . Application of 200-V peak-to-peak sine input at 10 Hz to the vertical  $z$  piezoactuators gives approximately 1  $\mu\text{m}$  of travel. Over these ranges, the measured  $x/y$  cross coupling is 75-nm peak-to-peak (1.83% or  $-34.75$  dB) in  $y$  caused by actuating the  $x$  piezo and 24-nm peak-to-peak (0.6% or  $-44.44$  dB) in  $x$  caused by actuating the  $y$  piezo. The measured vertical runouts are 27.6-nm peak-to-peak (0.35% or  $-49.2$  dB) caused by actuating the  $x$  piezo and 81.4-nm peak-to-peak (0.97% or  $-40.3$  dB) caused by actuating the  $y$  piezo. It is noted that the lateral  $x$ -to- $y$  and  $y$ -to- $x$  cross coupling may be caused by the  $y$ -stage's compliance. For example,  $x$ -actuation may cause slight deformation in the  $y$ -stage body leading to measured cross coupling. Similarly, lateral-to-vertical cross coupling ( $x$ -to- $z$  and  $y$ -to- $z$ ) may be caused by a tilted sample or misalignment of the displacement sensor, e.g., when the tilted sample translates laterally, the tilted surface may appear to move vertically relative to a fixed sensor.

Frequency response functions are measured using a dynamic signal analyzer (Stanford Research Systems SRT785). Small inputs ( $<70$  mV) are applied to the piezo amplifiers during the test to minimize the effect of nonlinearity such as hysteresis. Measurements for the  $x$ - and  $y$ -stages are taken with both the stage mounted sensors (inductive sensor for  $x$ , and capacitive

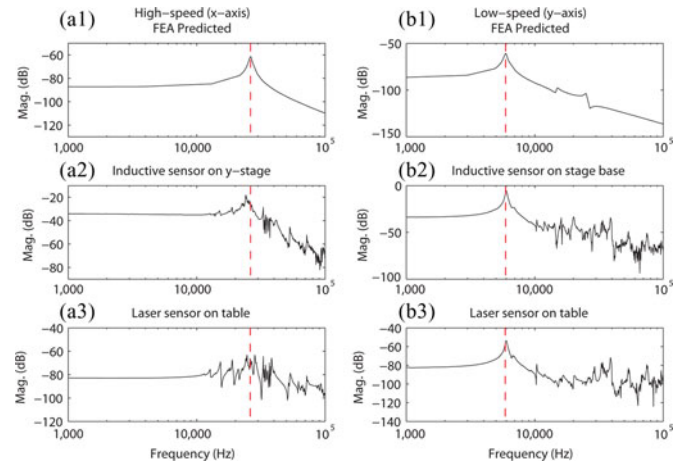


Fig. 12. (a1)–(a3) Comparison of predicted and measured frequency response functions for the high-speed stage ( $x$ -axis), (b1)–(b3) low-speed stage ( $y$ -axis). The vertical dashed line is used to compare the experimentally measured results to the FEA predicted first resonance peak.

sensor for  $y$ ) and again with a single-point laser vibrometer (Polytec CLV-1000 with CLV-800-vf40 laser unit) mounted to the vibration isolation table (for both  $x$  and  $y$ ). The measured responses are shown in Fig. 12 along with the FEA predictions. When measured relative to the  $y$ -stage body, the  $x$ -stage has a dominant first resonance peak at 24.2 kHz (a2) which matches well with the predicted value of 25.9 kHz (a1). Several small pole/zero pairs appear before the dominant peak. However, when measured using a laser vibrometer relative to an outside body such as the vibration isolation table (a3), the response shows additional unexpected resonances. These peaks are thought to be due to modes in the  $y$ -stage being excited by the  $x$ -stage. Unfortunately, these modes are not detectable when the sensor is attached to the  $y$ -stage body. The measured dominant resonance for the  $y$ -stage at 6.0 kHz both measured using the capacitive displacement sensor attached to the stage body (a2) and the laser vibrometer on table (a3) matches the predicted FEA value (a1) at 5.96 kHz very well. Not only do the dominant resonances agree with the FEA results, they are also piston modes relative to their mounting point as designed and predicted by FEA. The frequency response for the  $z$ -axis is measured using the deflection of a 360-kHz tapping-mode AFM cantilever (Vista Probes T300 www.vistaprobes.com) in contact-mode over the sample surface. The dominant resonance is approximately 70 kHz in the actuation (piston) mode.

### V. CONTROL

Due to the hysteresis and creep behaviors in the piezo-stack actuators and the inherent structural dynamics, control is required for precision positioning, especially at high scan frequencies [2], [25]. Unfortunately, one control method cannot cover the full operating range and frequency of the stage. Therefore, four methods to control the actuation of the stage in the lateral directions are investigated: 1) open loop with smooth inputs; 2) PID feedback control (which is the industry standard); 3) discrete-time repetitive control (RC); and 4) model-based

<sup>1</sup>LabView EASyLab SPM Interface is available by contacting the corresponding author (K. Leang, e-mail: kam@unr.edu).

feedforward control. For example, for low-speed operation (less than 100 Hz), PID and RC control offer excellent performance by compensating for hysteresis nonlinearity. As the scanning speed increases, both open loop with smooth inputs and inversion-based feedforward control are needed to compensate for the dynamics effects. Feedforward control is useful for achieving video-rate SPM. In the end, the user selects a controller based on the operating range and frequency and the required precision. Also, the complexity of the controller should be considered as more time may be required to appropriately tune a given controller.

### A. Open-Loop Smooth Input Signal

Nanopositioners used in SPM systems for scanning applications are commonly driven by triangle input signals. Such a signal is used because it causes the stage to move with constant velocity. However, a triangle input signal can excite the dynamics of the stage due to the sharp turn-around points. To minimize this, a smooth triangle input signal consisting of ten harmonic terms is created to control the positioning along the  $x$ -direction. A summary of other input-shaping techniques that can be applied with the same objective is discussed in [26].

### B. Analog PID Control

At low frequencies, PID control is robust and effective for minimizing creep and hysteresis, as well as to improve dynamic performance. A recently proposed force-feedback controller is another attractive approach [27]. An analog PID controller, with transfer function  $C(s) = U(s)/E(s) = k_p + k_i/s + k_d s$ , is designed to control the positioning along the lateral directions. Fig. 13 shows the block diagram and fabricated board based on the Linear Technology LT1362 high-speed operational amplifier. The board is designed to accommodate feedforward inputs  $u_1$ ,  $u_2$ , and  $u_{ff}$ , for implementing integrated controllers [28]. The PID gains are tuned using a dynamics model of the positioning stage. For example, the measured frequency response functions shown in Fig. 12 are curve fitted to linear transfer function models using the system identification toolbox in MATLAB. For the low-speed axis  $y$ , the derivative term is omitted ( $k_d = 0$ ) and integral control is used with a gain of approximately  $k_i = 30,000$ . The measured bandwidth ( $-3.01$  dB cutoff) of the controller in the  $y$ -direction is 300 Hz. For the  $x$ -axis, the PID gains are tuned to  $k_p = 1.2$ ,  $k_i = 1 \times 10^5$ , and  $k_d = 1 \times 10^{-5}$ ; the closed-loop bandwidth is 2.5 kHz.

### C. FPGA-Based Discrete-Time Repetitive Control

For relatively low-speed positioning, PID control is adequate. However, as the scanning speed increases, significant tracking error exists due to dynamic effects. To improve the tracking precision for scanning applications in which the desired trajectory is periodic, repetitive control is added to PID and demonstrated on the high-speed  $x$ -axis.

Repetitive control is based on the Internal Model Principle, where a signal generator is incorporated into a feedback control loop for tracking periodic reference trajectories [29]. In SPM

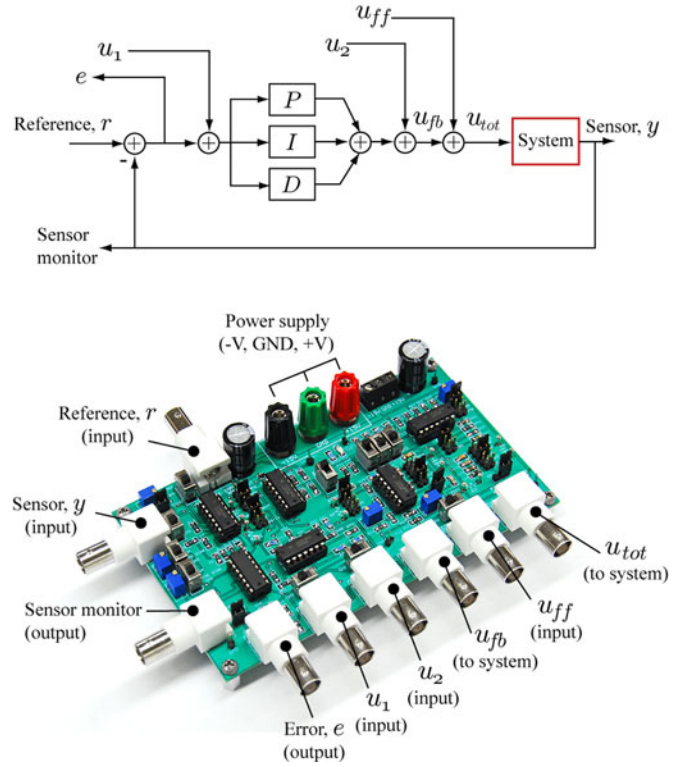


Fig. 13. Custom-designed analog PID feedback controller board. Two boards are used to control the  $x$ - and  $y$ -axes.

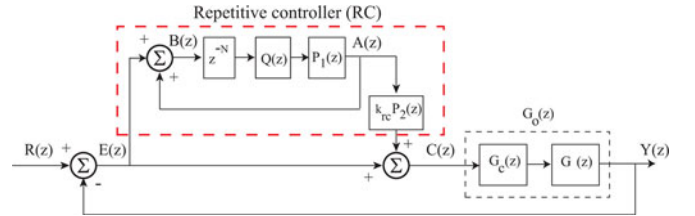


Fig. 14. Repetitive control for nanopositioning: a plug-in RC with phase-lead compensators,  $P_1(z)$  and  $P_2(z)$ , to enhance performance.

applications such as imaging and patterning, the reference signal is periodic and the scanning period is often known in advance. Therefore, RC can be used effectively to reduce the tracking error from one operating cycle to the next.

The block diagram of the plug-in RC is shown in Fig. 14, where a signal generator with period  $T_p$  is created by a positive feedback loop and pure delay  $z^{-N}$ . The positive integer  $N = T_p/T_s \in \mathbb{N}$  is the number of points per period of the reference trajectory  $r(t)$  and  $T_s$  is the sampling period. The plant (i.e., piezo-stack actuator and flexures) is assumed to be linear and represented by  $G(z)$ , where  $z = e^{j\omega T_s}$ ,  $\omega \in (0, \pi/T_s)$ . The PID controller is represented by  $G_c(z)$ . The low-pass filter  $Q(z)$  in the RC block provides robustness by reducing the effects of high gain at high frequencies. The parameters for the RC include the RC gain  $k_{rc}$  and two phase-lead compensators  $P_1(z) = z^{m_1}$  and  $P_2(z) = z^{m_2}$ , where  $m_1$  and  $m_2$  provide a linear phase lead (in units of radians) of  $\theta_{1,2}(\omega) = m_{1,2}T_s\omega$ , for  $\omega \in (0, \pi/T_s)$ . The two phase-lead compensators can be adjusted to compensate for the phase lag in the closed-loop system to improve the tracking

performance. By inspection, the transfer function of the signal generator that relates  $E(z)$  to  $A(z)$  in Fig. 14 is given by

$$\frac{A(z)}{E(z)} = \frac{Q(z)P_1(z)z^{-N}}{1 - Q(z)P_1(z)z^{-N}} = \frac{Q(z)z^{(-N+m_1)}}{1 - Q(z)z^{(-N+m_1)}}. \quad (15)$$

In the absence of the low-pass filter  $Q(z)$  and positive phase lead  $P_1(z) = z^{m_1}$ , the poles of the signal generator are  $1 - z^{-N} = 0$ , which implies infinite gain at the harmonics of the periodic reference trajectory. Such large gain is what gives the RC its ability to track periodic trajectories. However, practical RC design requires a low-pass filter  $Q(z)$  because the large gain at high frequencies can lead to instability of the closed-loop system. For simplicity, a standard low-pass filter of the form  $Q(z) = a/z + b$ , where  $|a| + |b| = 1$ , is chosen. The cut-off frequency of the low-pass filter is set to 7 kHz. Alternatively, a zero-phase filter can also be considered [30].

The stability of the RC system is presented as follows. Let  $H(z) = Q(z)z^{(-N+m_1)}$  and  $G_0(z) = G_c(z)G(z)$ . It is assumed that (1) the reference trajectory  $R(z)$  is periodic and (2) the closed-loop system without the RC loop is asymptotically stable, i.e.,  $1 + G_c(z)G(z) = 0$  has no roots outside of the unit circle in the  $z$ -plane. The stability is shown by applying the Small Gain Theorem [31]. First, the transfer function relating the reference trajectory  $R(z)$  and the tracking error  $E(z)$  is

$$S_{rc}(z) = \frac{E(z)}{R(z)} = \frac{[1 - H(z)]S(z)}{1 - H(z)[1 - k_{rc}P(z)G_0(z)S(z)]} \quad (16)$$

where  $S(z) = 1/(1 + G_0(z))$  is the sensitivity function of the feedback system without the repetitive controller. Furthermore, let  $T(z)$  represent the complimentary sensitive function of the closed-loop feedback system without RC, that is,  $T(z) = G_0(z)S(z)$ . Since  $S(z)$  has no poles outside the unit circle in the  $z$ -plane, it is stable. Replacing  $z = e^{j\omega T_s}$ , and since  $1 - H(z)$  is stable, the closed-loop system is asymptotically stable when

$$\begin{aligned} & |H(z)[1 - k_{rc}P_2(z)G_0(z)S(z)]| \\ & = |H(e^{j\omega T_s})[1 - k_{rc}e^{j\theta_2(\omega)}G_0(e^{j\omega T_s})S(e^{j\omega T_s})]| < 1 \end{aligned} \quad (17)$$

for all  $\omega \in (0, \pi/T_s)$ , where the phase lead  $\theta_2(\omega) = m_2 T_s$ . Observing that  $|Q(e^{j\omega T_s})| \leq 1$  and replacing the complimentary sensitive function of the closed-loop system without RC with  $T(e^{j\omega T_s}) = A(\omega)e^{j\theta_T(\omega)}$ , where  $A(\omega) > 0$  and  $\theta_T(\omega)$  are the magnitude and phase of  $T(e^{j\omega T_s})$ , respectively, (17) can be simplified to  $|1 - k_{rc}A(\omega)e^{j[\theta_T(\omega) + \theta_2(\omega)]}| < 1$ . Therefore, the following conditions must be met for a stable closed loop:

$$0 < k_{rc} < 2 \cos[\Theta(\omega)]/A(\omega), |\Theta(\omega)| < \pi/2 \quad (18)$$

where  $\Theta(\omega) = \theta_T(\omega) + \theta_2(\omega)$ . The RC is implemented using FPGA hardware, National Instruments cRIO-9002, with  $N = 100$  (points per period),  $m_1 = 6$ ,  $m_2 = 0$ , and closed-loop sampling frequency of 100 kHz. The lead parameters  $m_1$  and  $m_2$  were chosen by simulating the response of the RC such that the lowest simulated tracking error was achieved. The RC gain is chosen as  $k_{rc} = 0.95$  to satisfy the stability conditions given in (18). A second-order linear dynamics model  $G(s)$  was obtained by curve fitting the measured frequency response (Bode

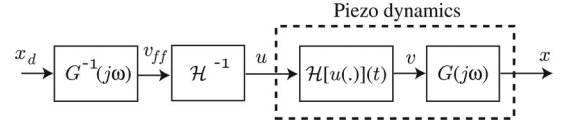


Fig. 15. The inversion-based feedforward control approach [2], [25].

plot) using MATLAB and used for simulating the response of the controller. The input to the piezoactuator for identification was kept small (50 mV) to avoid the effects of hysteresis. The linear dynamics model is given by

$$G(s) = \frac{2.805 \times 10^9}{s^2 + 2.87 \times 10^4 s + 2.30 \times 10^{10}}. \quad (19)$$

A discrete-time model  $G(z)$  was determined by converting  $G(s)$  using MATLAB's `c2d` function with a sampling frequency of 100 kHz. Additional details of RC design for SPM can be found in [31].

#### D. Feedforward Hysteresis and Dynamic Compensation

Model-based feedforward control is effective at compensating for both hysteresis and dynamic effects at high scan frequencies [2], [25]. Since during scanning, the  $x$ -axis is operated at high frequencies, both dynamic and hysteresis feedforward compensation are applied to this axis (see Fig. 15). Closed-loop integral control is used for the low-speed  $y$ -axis to minimize hysteresis and creep effect. To minimize excitation of high-order dynamics and out-of-plane modes along the  $x$ -axis, the desired output trajectory  $x_d(t)$  is chosen as a sine wave and the inversion-based approach is used to determine the feedforward input, specifically

$$V_{ff}(j\omega) = G(j\omega)^{-1}X_d(j\omega) \quad (20)$$

where  $G(j\omega)^{-1}$  is the inverse of the plant dynamics and  $X_d(j\omega)$  is the Fourier transform of the desired output trajectory. The inverse of the plant is determined from the measured frequency response function for the  $x$ -direction [see Fig. 12(a2)]. In general, the time-domain solution to the feedforward input  $v_{ff}(t)$  is computed by the inverse Fourier transform of  $V_{ff}(j\omega)$ .

Afterward, the dynamics-compensated feedforward input  $v_{ff}(t)$  is used as an input to a hysteresis feedforward compensator  $\mathcal{H}^{-1}[\cdot]$ . The compensator is based on the Prandtl-Ishlinskii (P-I) model [32]. One of the advantages of the P-I model over other hysteresis models such as the Preisach model is the smaller number of parameters that need to be identified, and as a result, the model is more computationally efficient for real-time applications [32]. Particularly, an inverse of the P-I model is proposed based on the observation of the shape of the input versus output curve shown in Fig. 16(a) ( $u$  versus  $v$  plot). For such a curve, the inverse-play-type operator shown in Fig. 16(b) is proposed for constructing the inverse model. The inverse-play operator is described by  $\mathcal{P}_{inv,r'}[v](0) = p_{inv,r'}(h(0), 0) = 0$ , with  $\mathcal{P}_{inv,r'}[v](t) = p_{inv,r'}(h(t_i), \mathcal{P}_{inv,r'}[h](t_i))$ , where  $p_{inv,r'}(h(t), p_{inv,r'}[h](t_i)) = \max(-h - r', \min(-h + r', p_{inv,r'}[h](t_{i-1})))$  and  $r'$  denotes the threshold of the inverse-play operator. Then, the output of the inverse hysteresis model is

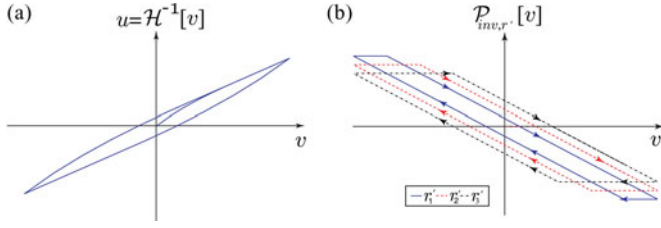


Fig. 16. The P-I model: (a) measured input versus output (hysteresis) curve; (b) play-type operator for the inverse model with threshold  $r'$ .

given by

$$\mathcal{H}^{-1}[v](t) \triangleq k_{\text{inv}} h(t) + \int_0^R d_{\text{inv}}(r') \mathcal{P}_{\text{inv}, r'}[v](t) dr'. \quad (21)$$

The function  $h(t) = g'_0 v(t) + g'_1$ , where  $v(t)$  is the output of the hysteresis behavior and  $g'_0$  and  $g'_1$  are constants. The parameters for the inverse model are obtained by curve fitting the measured I/O data (hysteresis curve) using the nonlinear least-squares optimization toolbox in MATLAB. The applied input for identification was a 1-Hz triangular signal that varied in amplitude from 100 mV to full-scale (10 V) and the displacement of the stage was measured for identifying the hysteresis nonlinearity. Specifically, the density function is chosen as  $d_{\text{inv}}(r') = \lambda' e^{-\delta' r'}$ , where  $r' = \rho' j$ , for  $j = 1, 2, \dots, 8$ . The parameters are determined as  $g'_0 = 2.7742$ ,  $g'_1 = -0.0123$ ,  $\lambda' = 0.0211$ ,  $\delta' = -3.851$ ,  $\rho' = 0.1322$ , and  $k' = 1$ .

## VI. TRACKING AND AFM IMAGING RESULTS

Tracking and AFM imaging results are presented to demonstrate the performance of the control methods and capabilities of the positioning stage. The following approaches are evaluated for the fast-scan direction ( $x$ -axis): 1) open-loop triangle input (OL); 2) open-loop smooth triangle input (ST); 3) PID control (FB); 4) repetitive control (RC); 5) dynamic and hysteresis feedforward control (FF); and 6) sine-wave feedforward control (SF).

As mentioned, a commercial AFM head is mounted on the top of the three-axis stage for the AFM imaging experiments (see Fig. 11). It is pointed out that the maximum operating scan frequency of the commercial AFM is less than 10 Hz. A calibration sample with 3- $\mu\text{m}$  pitch, 20-nm tall features is attached to the sample stage using a strong adhesive (cyanoacrylate-based fast-acting adhesive). Gluing is preferred to minimize relative motion between the sample and sample platform. It is determined that commonly used double-side tape is not adequate for securing the sample for high-speed operation. A noncontact-mode AFM cantilever with a resonance of 360 kHz is used for contact-mode imaging. The AFM head used for imaging is only compatible with cantilevers with alignment grooves. Therefore, only a select group of cantilevers could be used for imaging. The 360-kHz noncontact cantilever is considered the best choice for the experiments. The gains for the vertical PI controller to maintain tip-to-sample contact are set relatively low for constant-height imaging. Images are created by plotting the measured cantilever deflection with respect to the desired

TABLE IV  
STEADY-STATE TRACKING ERROR RESULTS FOR  $x$ -AXIS SCANNING

CTR	$\epsilon_{\text{max}}$ (%)				$\epsilon_{\text{rms}}$ (%)			
	100 (Hz)	500 (Hz)	1000 (Hz)	2000 (Hz)	100 (Hz)	500 (Hz)	1000 (Hz)	2000 (Hz)
OL	9.7	12.0	14.5	20.6	6.0	8.1	10.7	15.7
ST	9.9	11.6	15.1	20.2	6.1	8.1	10.8	16.0
FB	2.8	10.0	19.3	37.3	1.4	6.8	13.9	29.2
RC	2.7	2.74	3.7	6.8	0.6	0.8	1.2	2.7
FF	3.9	4.8	5.7	6.9	1.6	2.4	3.0	3.7
SF	3.0	4.2	4.5	4.9	0.9	1.8	2.4	2.5

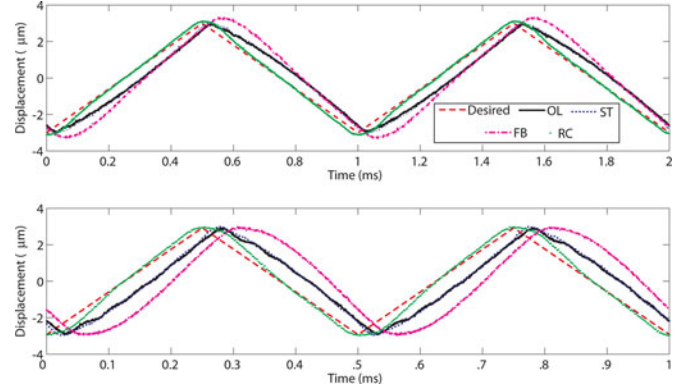


Fig. 17. Measured tracking results: (a) 1 kHz and (b) 2 kHz for open-loop (OL), smooth triangle (ST), PID feedback (FB), and repetitive control (RC).

lateral position of the AFM probe. Tracking and imaging results were acquired using the custom-designed LabView SPM program with high-speed data acquisition hardware.

The maximum and root-mean-squared tracking error (as a percentage of the total displacement range) for different scan frequencies are listed in Table IV. The tracking performance at 1 and 2 kHz is shown in Fig. 17. Finally, AFM images acquired at different scan frequencies are compared in Fig. 18. In the images shown, height is shown as variances in color, specifically low points (flat valleys) are dark while high points (flat plateaus) are light. The color variances in constant height features, such as the vertical bands on the flat plateaus and valleys seen in the open-loop images greater than 100 Hz, are likely caused by vertical motion of the sample relative to the static AFM head. Curvature or waviness is caused by lateral  $x/y$  tracking error, e.g., at low speed the curved features are caused by the hysteresis effect.

First, there is an obvious advantage with the high-speed stage compared to the performance of the commercial AFM scanner. For the newly developed scanner, the image is still ripple-free at 100-Hz scan frequency [see Fig. 18(a1)], a factor of 10 higher than the commercial scanner. Dynamic effects begin to show at 500 Hz [see Fig. 18(a2)]. Distortion due to hysteresis which causes the parallel features to appear curved represents the major source of tracking error. With increasing frequency under open-loop control with a pure triangle input signal (OL), the tracking errors shown in Table IV and Fig. 17 are excessively large at 14.5% and 20.6% at 1 and 2 kHz, respectively. Improvement in the image quality is achieved by applying a smooth triangle input (ST) as shown in Fig. 18(b1)–(b4). However, the smooth triangular input did not lower the tracking error significantly compared to a regular triangle input. Therefore, the majority of

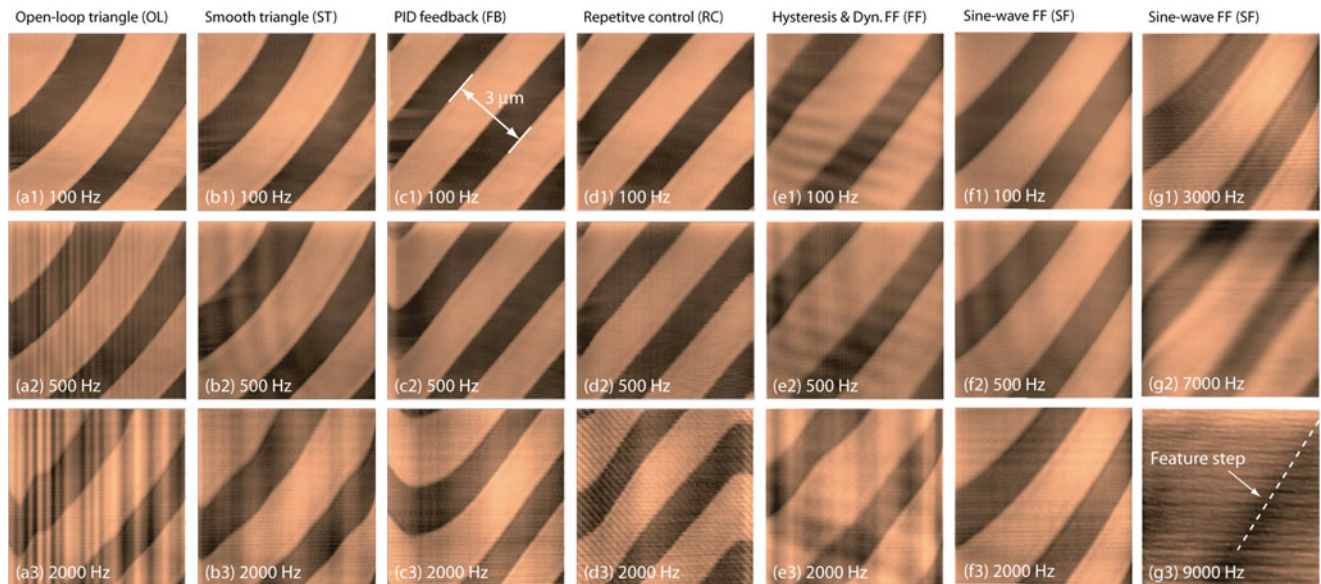


Fig. 18. AFM images of a calibration sample with 3- $\mu\text{m}$  pitch and 20-nm tall features.

the ripples for the triangle input case may also be caused by exciting the vertical modes.

Under PID control, the maximum tracking error at 100 and 500 Hz scanning is 2.8% and 10.0%, respectively (see Table IV). The hysteresis distortion is minimized by the PID feedback controller, as expected. However, above 1 kHz the error is significantly larger than the previous cases (see Fig. 17), indicating that the controller offers marginal performance at high speeds.

With RC, the tracking error is reduced significantly to 2.7% at 100 Hz and 6.8% at 2 kHz (see Fig. 17). The AFM images show very low distortion at 100 and 500 Hz. However, the trajectory was significantly rounded at 1- and 2-kHz scan rates due to the low-pass filter  $Q(z)$  used to ensure robustness. Additionally, high-frequency ripples in the image are observed at 2 kHz scanning, possibly caused by exciting the vertical and unexpected modes in the stage.

The feedforward approach for hysteresis and dynamics compensation shows better performance compared to the two previous open-loop cases, where the error is less than 10% up to 2-kHz scanning. The AFM images [see Fig. 18(e1)–(e4)] for this case show a reduction in distortion due to hysteresis as well as the dynamic effect (i.e., phase delay). Above 2 kHz, the feedforward approach (20) based on a sine-wave desired trajectory (without hysteresis compensation) is applied. The AFM images in Fig. 18(g1)–(g3) demonstrate the stage's capabilities for AFM imaging with line rates up to 7 kHz. A reduced-range image (approximately  $1\ \mu\text{m} \times 1\ \mu\text{m}$ ) at 9 kHz presented in Fig. 18(g4) shows that the feature step is distinguishable in the image. This scanning rate represents the upper limit of the stage. With cantilevers optimized for high-speed AFM, such as high resonance and low stiffness cantilevers, higher quality images can be obtained using the newly designed stage.

## VII. CONCLUSION

A three-axis serial-kinematic nanopositioning stage is developed with mechanical resonances in the kilohertz range for high-

speed applications. Double-hinged serial-flexures are used to guide the motion of the  $x$ - and  $y$ -stages and to enhance the stiffness in the out-of-plane direction, thus minimizing the effects of out-of-plane modes. The measured and predicted dynamic responses are in good agreement. AFM images acquired at line rates up to 7 kHz are presented. At this line rate, 70 frames/s AFM video with  $100 \times 100$  pixels resolution can be achieved.

## ACKNOWLEDGMENT

The authors would like to thank P. Leang for his insights and help with developing the LabView GUI front-end for high-speed AFM imaging. They are also grateful to Dr. A. J. Fleming for the insightful discussions and providing a PiezoDrive amplifier for the experiments.

## REFERENCES

- [1] T. Ando, T. Uchihashi, and T. Fukuma, "High-speed atomic force microscopy for nano-visualization of dynamic biomolecular processes," *Prog. Surf. Sci.*, vol. 83, nos. 7–9, pp. 337–437, 2008.
- [2] G. M. Clayton, S. Tien, K. K. Leang, Q. Zou, and S. Devasia, "A review of feedforward control approaches for nano precision positioning in high speed SPM operation," *Trans. ASME, J. Dyn. Syst. Meas. Cont.*, vol. 131, pp. 061101-1–061101-19, 2009.
- [3] B. Bhikkaji, M. Ratnam, A. J. Fleming, and S. O. R. Moheimani, "High-performance control of piezoelectric tube scanners," *IEEE Trans. Control Syst. Technol.*, vol. 15, no. 5, pp. 853–866, Sep. 2007.
- [4] G. Schitter and A. Stemmer, "Identification and open-loop tracking control of a piezoelectric tube scanner for high-speed scanning-probe microscopy," *IEEE Trans. Control Syst. Technol.*, vol. 12, no. 3, pp. 449–454, May 2004.
- [5] G. Schitter, W. F. Rijkee, and N. Phan, "Dual actuation for high-bandwidth nanopositioning," in *Proc. IEEE Conf. Decision Control*, Cancun, NM, 2008, pp. 5176–5181.
- [6] A. J. Fleming, "High-speed vertical positioning for contact-mode atomic force microscopy," in *Proc. IEEE/ASME Int. Conf. Adv. Intell. Mechatron.*, Singapore, 2009, pp. 522–527.
- [7] O. M. E. Rifai and K. Youcef-Toumi, "Coupling in piezoelectric tube scanners used in scanning probe microscopes," in *Proc. Amer. Control Conf.*, 2001, vol. 4, pp. 3251–3255.
- [8] M. J. Rost, L. Crama, P. Schakel, E. van Tol, G. B. E. M. van Velzen-Williams, C. F. Overgawu, H. ter Horst, H. Dekker, B. Okhuijsen,

- M. Seynen, A. Vijftigschild, P. Han, A. J. Katan, K. Schoots, R. Schumm, W. van Loo, T. H. Oosterkamp, and J. W. M. Frenken, "Scanning probe microscopes go video rate and beyond," *Rev. Sci. Instrum.*, vol. 76, no. 5, pp. 053710-1–053710-9, 2005.
- [9] L. M. Picco, L. Bozec, A. Ulcinas, D. J. Engledew, M. Antognozzi, M. A. Horton, and M. J. Miles, "Breaking the speed limit with atomic force microscopy," *Nanotechnology*, vol. 18, no. 4, pp. 044030-1–044030-4, 2007.
- [10] F. E. Scire and E. C. Teague, "Piezodriven 50- $\mu\text{m}$  range stage with subnanometer resolution," *Rev. Sci. Instrum.*, vol. 49, no. 12, pp. 1735–1740, 1978.
- [11] K. K. Leang and A. J. Fleming, "High-speed serial-kinematic AFM scanner: Design and drive considerations," *Asian J. Control*, vol. 11, no. 2, pp. 144–153, 2009.
- [12] G. Schitter, P. J. Thurner, and P. K. Hansma, "Design and input-shaping control of a novel scanner for high-speed atomic force microscopy," *Mechatronics*, vol. 18, no. 5–6, pp. 282–288, 2008.
- [13] Y. K. Yong, S. S. Aphale, and S. O. R. Moheimani, "Design, identification, and control of a flexure-based xy stage for fast nanoscale positioning," *IEEE Trans. Nanotechnol.*, vol. 8, no. 1, pp. 46–54, Jan. 2009.
- [14] Y. Li and Q. Xu, "A novel design and analysis of a 2-DOF compliant parallel micromanipulator for nanomanipulation," *IEEE Trans. Autom. Sci. Eng.*, vol. 3, no. 3, pp. 248–254, Jul. 2006.
- [15] Y. Li and Q. Xu, "Design and analysis of a totally decoupled flexure-based XY parallel micromanipulator," *IEEE Trans. Robot.*, vol. 25, no. 3, pp. 645–657, Jun. 2009.
- [16] J. H. Kindt, G. E. Fantner, J. A. Cutroni, and P. K. Hansma, "Rigid design of fast scanning probe microscopes using finite element analysis," *Ultramicroscopy*, vol. 100, nos. 3–4, pp. 259–265, 2004.
- [17] P. Gao, S. M. Swei, and Z. J. Yuan, "A new piezodriven precision micropositioning stage utilizing flexure hinges," *Nanotechnol.*, vol. 10, no. 4, pp. 394–398, 1999.
- [18] S. P. Timoshenko, *History of Strength of Materials*. New York: McGraw-Hill, 1953.
- [19] N. Lobontiu, *Compliant Mechanisms Design of Flexure Hinges*. Boca Raton, FL: CRC Press, 2003.
- [20] R. R. J. Craig, *Mechanics of Materials*, 2nd ed. New York: Wiley, 2000.
- [21] W. C. Young and R. G. Budynas, *Roark's Formulas for Stress and Strain*, 7th ed. New York: McGraw-Hill, 2002.
- [22] S. R. Park and S. H. Yang, "A mathematical approach for analyzing ultra precision positioning system with compliant mechanism," *J. Mater. Process. Technol.*, vol. 164–165, pp. 1584–1589, 2005.
- [23] Q. Xu and Y. Li, "Structure improvement of an XY flexure micromanipulator for micro/nano scale manipulation," in *Proc. 17th World Congr. Int. Fed. Autom. Control (IFAC)*, 2008, vol. 17, pp. 12733–12738.
- [24] S. Awatar and A. H. Slocum, "Constraint-based design of parallel kinematic XY flexure mechanisms," *J. Mech. Design*, vol. 129, no. 8, pp. 816–830, 2007.
- [25] K. K. Leang, Q. Zou, and S. Devasia, "Feedforward control of piezoactuators in atomic force microscope systems: Inversion-based compensation for dynamics and hysteresis," *IEEE Control Syst. Mag.*, vol. 29, no. 1, pp. 70–82, Feb. 2009.
- [26] A. J. Fleming and A. G. Wills, "Optimal periodic trajectories for band-limited systems," *IEEE Trans. Control Syst. Technol.*, vol. 13, no. 3, pp. 552–562, May 2009.
- [27] A. J. Fleming, "Nanopositioning system with force feedback for high-performance tracking and vibration control," *IEEE/ASME Trans. Mechatronics*, vol. 15, no. 3, pp. 421–432, Jun. 2010.
- [28] K. K. Leang and S. Devasia, "Feedback-linearized inverse feedforward for creep, hysteresis, and vibration compensation in AFM piezoactuators," *IEEE Trans. Control. Syst. Technol.*, vol. 15, no. 5, pp. 927–935, Sep. 2007.
- [29] T. Inoue, M. Nakano, and S. Iwai, "High accuracy control of a proton synchrotron magnet power supply," in *Proc. 8th IFAC World Congr.*, 1981, pp. 216–221.
- [30] M. Tomizuka, "Zero phase tracking algorithm for digital control," *Trans. ASME, J. Dyn. Syst. Meas. Control*, vol. 109, pp. 65–68, 1987.
- [31] U. Aridogan, Y. Shan, and K. K. Leang, "Design and analysis of discrete-time repetitive control for scanning probe microscopes," *Trans. ASME, J. Dyn. Syst. Meas. Control.*, vol. 131, pp. 061103-1–061103-12, 2009.
- [32] Y. Shan and K. K. Leang, "Repetitive control with Prandtl–Ishlinskii hysteresis inverse for piezo-based nanopositioning," in *Proc. Amer. Control Conf.*, St. Louis, MO, 2009, pp. 301–306.



**Brian J. Kenton** received the A.S. degree in engineering science from Hudson Valley Community College, Troy, NY, in 2001, and the B.S. degree in mechanical engineering from Clarkson University, Potsdam, NY, in 2003. He is currently a graduate student at the University of Nevada, Reno, where he is focusing on advanced mechanical design for nanopositioning systems.

From 2003 to 2007, he worked as a carpenter and expert drafting technician, and designed and manufactured snow skis.



**Kam K. Leang** (M'02) received the B.S. and M.S. degrees in mechanical engineering from the University of Utah, Salt Lake City, in 1997 and 1999, respectively, and the Ph.D. degree from the University of Washington, Seattle, in 2004.

Since 2008, he has been an Assistant Professor in the Department of Mechanical Engineering, University of Nevada, Reno. From 2005 to 2008, he taught in the Department of Mechanical Engineering, Virginia Commonwealth University, Richmond. His research interests include modeling and control of piezoactuators for scanning probe microscopy applications, fabrication and control of electroactive polymers, and design of microelectromechanical systems for nanotechnology.

Dr. Leang is a member of the ASME and SPIE.